ADVANCED OPTICAL MATERIALS
www.advopticalmat.de

Enhanced Light–Matter Interaction in ^{10}B Monoisotopic Boron Nitride Infrared Nanoresonators

*Marta Autore, Irene Dolado, Peining Li, Ruben Esteban, Francisco Javier Alfaro-Mozaz, Ainhoa Atxabal, Song Liu, James H. Edgar, Saül Vélez, Fèlix Casanova, Luis E. Hueso, Javier Aizpurua, and Rainer Hillenbrand**

Phonon-polaritons, mixed excitations of light coupled to lattice vibrations (phonons), are emerging as a powerful platform for nanophotonic applications. This is because of their ability to concentrate light into extreme sub-wavelength scales and because of their longer phonon lifetimes compared to their plasmonic counterparts. In this work, the infrared properties of phonon-polaritonic nanoresonators made of monoisotopic ^{10}B hexagonal boron nitride (h-BN) are explored, a material with increased phonon-polariton lifetimes compared to naturally abundant h-BN due to reduced photon scattering from randomly distributed isotopes. An average relative improvement of 50% of the quality factor of monoisotopic h-BN nanoresonators is obtained with respect to nanoresonators made of naturally abundant h-BN, allowing for the sensing of nanometric-thick films of molecules through both surface-enhanced absorption spectroscopy and refractive index sensing. Further, even strong coupling between molecular vibrations and the phonon-polariton resonance in monoisotopic h-BN ribbons can be achieved.

Dr. M. Autore, I. Dolado, Dr. P. Li, Dr. F. J. Alfaro-Mozaz, Dr. A. Atxabal, Prof. F. Casanova, Prof. L. E. Hueso, Prof. R. Hillenbrand
CIC nanoGUNE BRTA
Donostia-San Sebastián 20018, Spain
E-mail: r.hillenbrand@nanogune.eu

Dr. R. Esteban, Prof. J. Aizpurua
Donostia International Physics Center (DIPC)
Donostia-San Sebastián 20018, Spain

Dr. R. Esteban, Prof. F. Casanova, Prof. L. E. Hueso, Prof. R. Hillenbrand
IKERBASQUE
Basque Foundation for Science
Bilbao 48009, Spain

Dr. R. Esteban, Prof. J. Aizpurua
Centro de Física de Materiales (MPC, CSIC-UPV/EHU)
Donostia-San Sebastián 20018, Spain

Dr. S. Liu, Prof. J. H. Edgar
Tim Taylor Department of Chemical Engineering
Kansas State University
Manhattan, KS 66506, USA

Dr. S. Vélez
Department of Materials
ETH Zürich
Zürich 8093, Switzerland

Prof. R. Hillenbrand
Department of Electricity and Electronics
UPV/ EHU
Bilbao 48080, Spain

The ORCID identification number(s) for the author(s) of this article can be found under https://doi.org/10.1002/adom.202001958.

DOI: 10.1002/adom.202001958

1. Introduction

The emerging field of nanophotonics requires a broad range of low-loss sub-diffractional components for full light control and manipulation at the nanoscale, such as amplitude and phase modulators, waveguides, perfect absorbers, light generators, concentrators, and switches. Most of the research during the last decade has focused on plasmonic structures based on metals[1,2] and, more recently, on high refractive index dielectrics[3] and graphene.[4]

Phonon-polaritonic nanostructures made of polar crystals (SiC, h-BN, Quartz, etc.) represent a valuable platform for infrared nanophotonics due to their higher polaritonic quality (Q) factors as compared to their plasmonic counterparts and due to their high degree of electromagnetic field confinement.[5,6,7,8,9,10] This is achieved through the excitation of surface phonon-polaritons – mixed excitations of photons and crystal lattice vibrations – at frequencies where the real part of the dielectric function is negative (between the transverse optical (TO) and the longitudinal optical (LO) phonon frequencies, this frequency range being called the crystal's Reststrahlen band).

Recently, van der Waals materials have opened new opportunities for fabricating nanophotonic components[11] based on exfoliating atomically smooth flakes comprising only a few atomic layers. A prototypical example is hexagonal boron nitride (h-BN).[12] The layered nature of h-BN leads to a strong uniaxial anisotropy of its dielectric function, which is described by in-plane ($\varepsilon_{\parallel}$) and out-of-plane ($\varepsilon_{\perp}$) components. In its Reststrahlen bands, where $\mathrm{Re}(\varepsilon_{\parallel}) \cdot \mathrm{Re}(\varepsilon_{\perp}) < 0$, ultra-confined phonon-polaritons can propagate inside the volume of the material. Owing to their hyperbolic isofrequency surface in momentum space, they are called hyperbolic phonon-polaritons (HPhPs) and can posess negative phase and slow group velocities.[13] The intriguing potential of h-BN for mid-infrared nanophotonics has been recently unveiled by the fabrication of high-Q phonon-polariton resonators,[14,15] linear waveguides,[16] antennas,[17] and hyperbolic metasurfaces.[18] Moreover, h-BN nanoribbons have been used for surface-enhanced infrared absorption (SEIRA) spectroscopy,[19,20] where their high Q factor is beneficial for approaching strong coupling between HPhPs and molecular vibrations.[15]

Recently, Giles et al. substantially increased the propagation length and lifetime of phonon-polaritons in h-BN, by employing monoisotopic (isotopically pure) h-BN.[21] Indeed, while ^{14}N is 99.6% abundant, natural boron consists of ≈ 80% ^{11}B and ≈ 20% ^{10}B isotopes. The random distribution of boron isotopes (isotopic disorder) leads to increased phonon scattering in natural h-BN. Giles et al. showed that h-BN crystals with high isotope purities of 99.22 at% ^{10}B and 99.41 at% ^{11}B increased the lifetime of HPhPs propagating in thin h-BN flakes by factors between 1.4 and 1.8 depending on the frequency range. First-principle calculations predict that even higher increases are possible, as much as an order of magnitude. However, the influence of the increased lifetime on the Q factor of phonon-polaritonic resonators, which may be affected by fabrication-induced defects, is widely unexplored.

In this work we fabricated nanoribbon arrays made of monoisotopic h-BN (99.22 at% ^{10}B)[22] indicated as h-BN* in the following (see Experimental Section for details on crystal growth). By measuring far-field transmission spectra, we show an increase of the Q factor of the HPhPs' lowest order Fabry–Pérot resonance in h-BN* compared to the naturally abundant h-BN ribbon arrays, as well as the appearance of higher order modes. We further show that h-BN* nanoribbons can be used for simultaneous refractive index sensing and SEIRA spectroscopy of thin molecular layers. Importantly, the improvement in the Q factor of the HPhP resonances leads to strong coupling between phonon polaritons and molecular vibrations, which in recent experiments with naturally abundant h-BN was achieved only at its onset.[15]

2. Comparison Between Naturally Abundant and Monoisotopic h-BN Nanoresonators

To compare the infrared response of nanoresonators made of monoisotopic and naturally abundant h-BN, we fabricated several sets of ribbon arrays (with varying widths w nominally ranging from 140 to 200 nm, and a fixed period D = 400 nm) starting from mechanically exfoliated flakes of comparable thickness $d \approx 35$ nm. All the fabrication steps (mechanical flake exfoliation, electron beam lithography and chemical dry etching) were carried out at the same time and on the same substrate (a 10 × 10 × 1 mm^3 CaF_2 crystal), to avoid possible differences induced by changes in the fabrication process. In **Figure 1** we show the transmission spectra of natural (panel a) and monoisotopic (panel b) h-BN ribbons, measured by Fourier transform infrared (FTIR) spectroscopy (see Experimental Section). All spectra were measured in an N_2-purged box at room temperature and normalized to the bare substrate spectrum, T_0. The infrared light of normal incidence was polarized perpendicular to the ribbons, in order to excite the transverse Fabry–Pérot resonances of the HPhPs.[15]

The first order phonon-polariton Fabry–Pérot resonance appears as a pronounced dip in the spectra and blueshifts as the width of the ribbon decreases. Analysis of the measured spectra allows us to quantify the difference in the quality factor of resonances obtained with h-BN and h-BN* ribbon arrays. To that end, we fitted a Lorentzian line shape (see Experimental Section) to each spectrum to extract the resonance frequency ω_{HPhP} and full width at half maximum (FWHM), γ_{HPhP}, yielding the quality factors $Q = \frac{\omega_{\mathrm{HPhP}}}{\gamma_{\mathrm{HPhP}}}$ (shown in Figure 1c). They exhibit an overall improvement for the h-BN* ribbons, which, however, is not constant over the considered frequency range. At higher frequencies (ω > 1480 cm^{-1}), Q is consistently larger, amounting to an improvement of up to 70%. On the other hand, Q decreases with decreasing frequency, that is, for larger ribbon widths, which is counterintuitive as for larger widths the surface roughness or defects from the fabrication process should have less influence. To clarify our findings, we measured transmission spectra of ribbon arrays made of other h-BN* flakes (see Section S1, Supporting Information) and we partially observed the opposite tendency (i.e., that Q increases with decreasing frequency). We thus attribute the variations of the Q factor of h-BN* ribbons (and the irregular spectral shifts with decreasing resonator width seen in Figure 1c) to fabrication uncertainties, including variations in the ribbon width, non-vertical side walls, and surface roughness (see SEM images in Figure S1, Supporting Information), which become more detrimental when material-intrinsic losses decrease. However, and most important, the Q factors obtained for the h-BN* ribbons are higher than those of the h-BN ribbons for most measurements (and the statistical average). Our experiments thus reliably indicate that the lower intrinsic phonon damping of h-BN* yields the improved Q factor of the h-BN* nanoresonators.

3. Observation of Isolated Higher Order Modes in Thick Monoisotopic h-BN Nanoribbon Arrays

We performed transmission spectroscopy on a set of thicker h-BN* ribbon arrays (d = 90 nm), with fixed period D = 400 nm and several widths w. All spectra (**Figure 2**a) show a pronounced dip above 1500 cm^{-1} (marked α) and two smaller dips (marked β and γ) that shift to higher frequencies with decreasing width (from yellow to black spectrum), as highlighted by the blue dashed guide to the eyes. Interestingly, the β and γ dips possess higher Q factors of up to 310, although their intensity is lower than the fundamental (α) resonance (see Section S4, Supporting Information for details). We attribute the β and γ dips to higher-order HPhP modes (in the vertical z-direction, i.e., across the slab), as they appear at lower frequencies as compared to the fundamental mode. The observation of higher-order HPhP modes has been previously reported in h-BN nanostructures of thickness $d \geq 250$ nm,[14,23,24] which is more than a factor of 2 thicker than our resonators.

To better understand the nature of the resonances, we compare in Figure 2b an exemplary experimental spectrum (black curve) with a numerically simulated spectrum (green curve, see Experimental Section for details) for rectangular ribbons of the same width. The ribbon width in the simulation is w = 210 nm, which is the average of the widths measured at the top and bottom of the ribbons by atomic force microscopy (AFM). Both spectra exhibit the same behavior, but all dips in the simulated spectrum are blue-shifted compared to

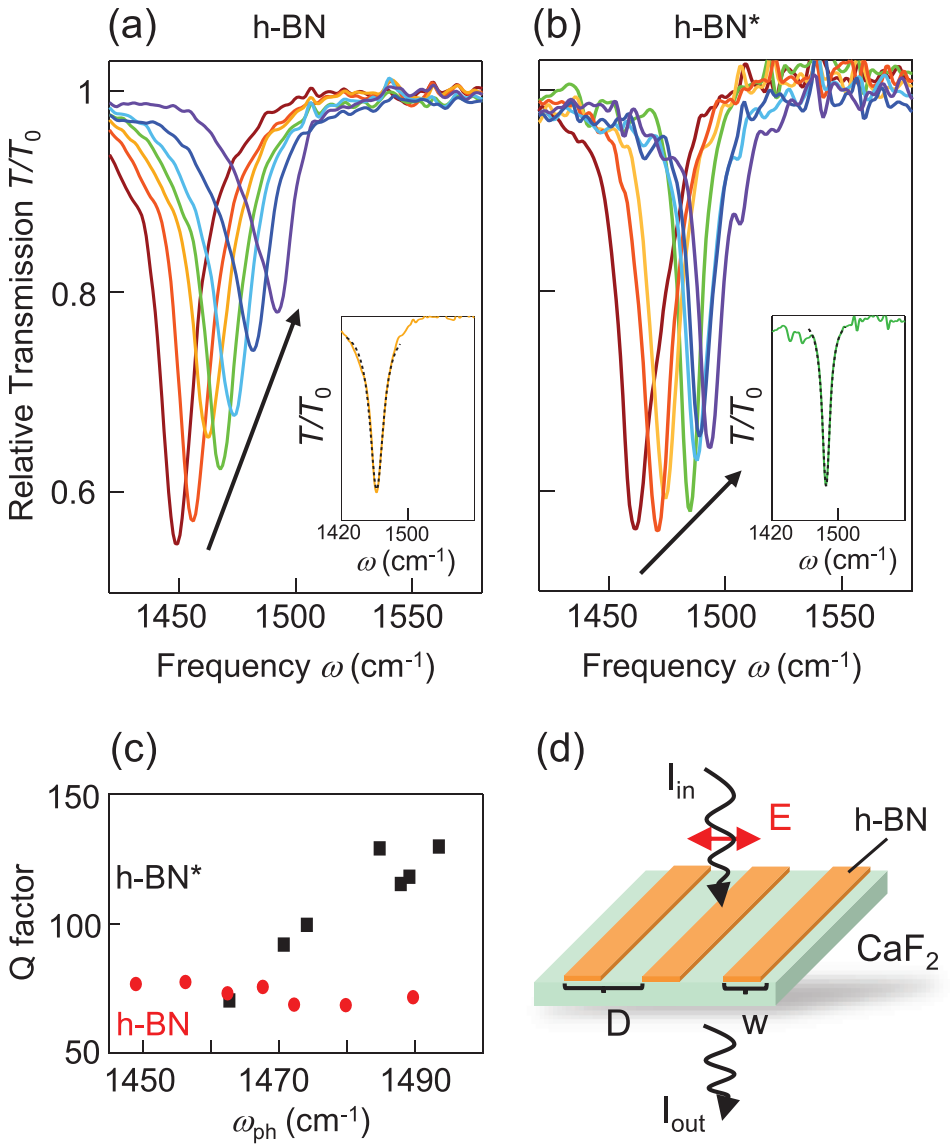

Figure 1. Relative transmission spectra of a) naturally abundant h-BN and b) monoisotopic h-BN* ribbon arrays (of areas of 20 × 20 µm and 30 × 30 µm) of varying width w, measured at normal incidence and polarization perpendicular to the ribbons. Nominal values of w ranging from 140 to 200 nm correspond to colors from purple to red (black arrow indicates decreasing w). Insets: exemplary transmission spectra (solid lines) and Lorentzian fits (dashed lines). c) Experimentally determined Q factor of each resonator, plotted as a function of the resonance frequency for h-BN (red dots) and h-BN* (black squares) ribbons. d) Sketch of the FTIR transmission experiment.

the corresponding experimental dips. A better agreement is reached by simulating spectra of a more realistic ribbon geometry, that is, a ribbon of trapezoidal cross section (red curve; top and bottom width of 140 and 280 nm, respectively, were measured by AFM). We note that the β and γ modes in the simulations possess extremely high Q factors (420 and 680, respectively), which are challenging to resolve in the experiment (where the spectral resolution is around 2 cm^{-1}).

To identify the modes associated to the resonance dips, we calculated the electric field distribution at the dip positions. The cross section of Re[E_z] for ribbons with trapezoidal and rectangular shapes is shown in Figure 2c and 2d, respectively. The rectangular shapes are useful to better understand the complex field pattern observed for the trapezoidal cross sections. We thus analyze first the field outside the rectangular ribbons (neglecting the complicated pattern inside the structures, which is due to the superposition of hyperbolic rays[16]). The effective charge profile corresponding to the observed modes is sketched in Figure 2e. We can clearly recognize the transversal structure of the modes in both the z- and x-direction. The number of nodes of Re[E_z] in the z-direction indicates the order j of the slab mode (we follow the notation of Ambrosio et al.[25] for unstructured h-BN slabs) that exhibits Fabry–Pérot resonances in the horizontal (x-) direction, whose order k is determined by the number of nodes of Re[E_z] in x-direction. Following this notation, we are able to identify and label with indices (j, k) the four main modes in the simulations, which lets us associate the experimentally

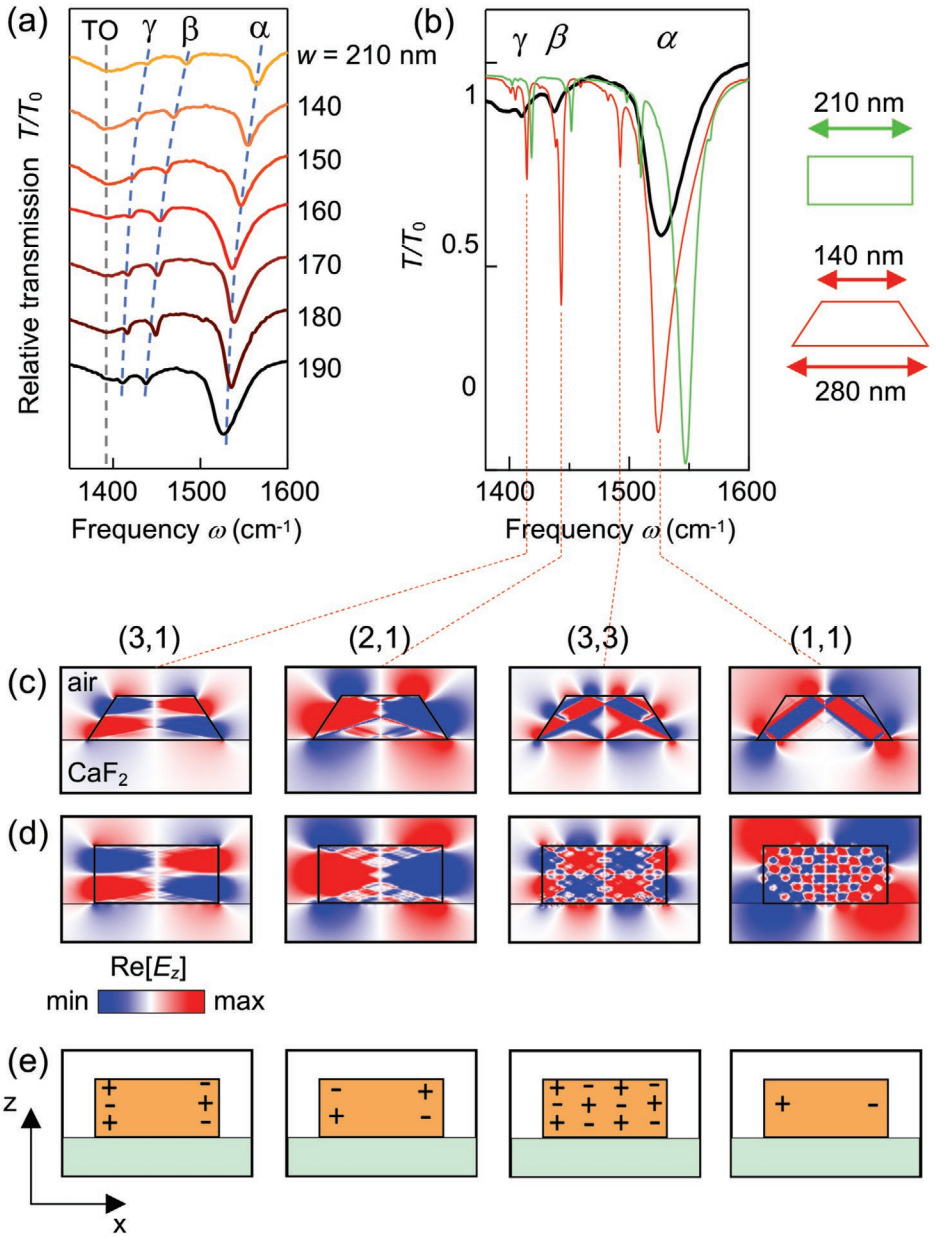

Figure 2. a) Relative transmission spectra of 90 nm-thick h-BN* ribbon arrays of several widths w, (nominally ranging from 130 nm, yellow, to 190 nm, black) with light linearly polarized perpendicular to the ribbons. α, β, and γ mark three dips corresponding to HPhP resonances. The curved blue dashed lines are guide to the eyes. The vertical grey dashed line indicates the TO phonon frequency. b) Comparison between a measured spectrum (black) and the simulated spectrum for rectangular (green, w = 210 nm) and trapezoidal (red) ribbons with 140 nm top and 280 nm bottom width. c,d) Simulations of the real part of the vertical component of the electric field, Re[Ez], for the dips of order (3,1), (2,1), (3,3), and (1,1) (from left to right, respectively) for the case of trapezoidal (c) and rectangular (d) ribbons (see Section S7, Supporting Information for details of the x component of the electric field, Re[Ex]). e) Sketch of the effective charge profile of the simulated modes in rectangular ribbons.

observed three dips α, β, and γ with the modes (1,1), (2,1), and (3,1), respectively. The mode (3,3), which is present in the simulations, is not present in the experimental spectra. For the ribbons with trapezoidal cross-section, we find that the mode structure (Figure 2c) of the corresponding dips matches that of the rectangular ribbons (i.e., has the same number of nodes in the x- and z- directions), although slightly distorted to match the modified boundaries of the resonator. From this analysis we can identify the experimentally observed β and γ dips as first order transverse Fabry-Pérot modes of higher order slab modes.

We note that the higher order modes can overlap with the broader fundamental mode, which might lead to asymmetric line shapes in case the modes cannot be resolved spectroscopically. For further discussion see Section S3, Supporting Information.

4. Simultaneous SEIRA and Refractive Index Sensing with Monoisotopic h-BN Resonators

h-BN* nanoresonators offer sensing possibilities that benefit both from the field enhancement on the resonators' surface and from the narrow linewidth of the resonances.[26] In the following we demonstrate their potential for simultaneous SEIRA spectroscopy[18,15] and refractive index (RI) sensing. The combination of the two sensing methodologies in the mid-IR has rarely been investigated up to now, despite promising initial experiments.[27,28,29,30,31]

For our experiments, we evaporated layers of the organic semiconductor 4,4′-bis(N-carbazolyl)-1,1′-biphenyl (CBP) on top of h-BN* ribbon arrays (see sketch in **Figure 3**d). Figure 3a,b show the spectra of two sets of arrays (ribbon widths $w = 230$ and 270 nm, indicating the average width of the trapezoidal ribbons obtained from AFM measurements), which were covered by CBP layers of several thicknesses (1, 3, 5, 10, 30, and 50 nm). The CBP molecule exhibits a vibrational mode at 1450 cm^{-1} (associated to a deformation of the C—H bond of the carbazole rings), as revealed by the dip in the reference transmission spectrum of a 30 nm thick CBP film on a bare CaF_2 substrate (red curves in Figure 3a–c). When the molecules are deposited onto the h-BN* ribbons, we first notice an increasing red-shift of the HPhP resonance with an increasing CBP thickness. With increasing spectral overlap between the HPhP and molecular resonances, we observe a strong modification of their line shapes that can be attributed to the coupling of the two modes.

For a quantitative analysis of the spectral shift of the HPhP mode and its coupling strength with the CBP molecular vibration, we applied the coupled harmonic oscillator model as described by Autore et al.,[15] where both the HPhP mode and the molecular vibration are described by single harmonic oscillators. Each of the two oscillators is described by an eigenfrequency ω_i, a damping parameter γ_i, and an effective driving force F_i that is proportional to the external electromagnetic field (the index i denotes either HPhP or CBP). They are coupled to each other through the coupling strength parameter g (see Section S5, Supporting Information for details). Note that although in the experimental transmission spectra one HPhP resonance dip may be a superposition of a strong fundamental HPhP mode and weaker higher order HPhP modes (see Section 2; Section S3, Supporting Information), the modelling of the HPhP resonator via a single harmonic oscillator can effectively describe the mode ensemble, analogously to the descriptions of multimodal light-matter interactions in quantum optics involving pseudo-modes[32] (i.e., a set of strongly overlapping resonator modes).

Fitting each spectrum of Figure 3b (fits are not shown), we determined the oscillator parameters. Note that the bare molecular vibrational eigenfrequency ω_{CBP} and damping parameter γ_{CBP} were fixed according to the CBP dielectric function (see Sections S5 and S6 of Supporting Information). By subsequently setting $g = 0$, we can reconstruct the transmission spectra of the bare (uncoupled) HPhP resonator, $\frac{T_{HPhP}}{T_0}$, which are plotted as orange curves in Figure 3b. Note that the coupled harmonic oscillator model takes into account the non-dispersive part of the dielectric function of CBP ($\varepsilon_\infty = 2.8$) separately from the vibrational contribution, thus yielding the shift of the bare HPhP resonance to lower frequencies with increasing CBP thickness. In other words, the reconstructed spectra of the bare HPhP resonance (orange curves) correspond to that of a HPhP resonator embedded in a dielectric environment described by ε_∞ solely, that is, in the absence of CBP molecular vibrations.

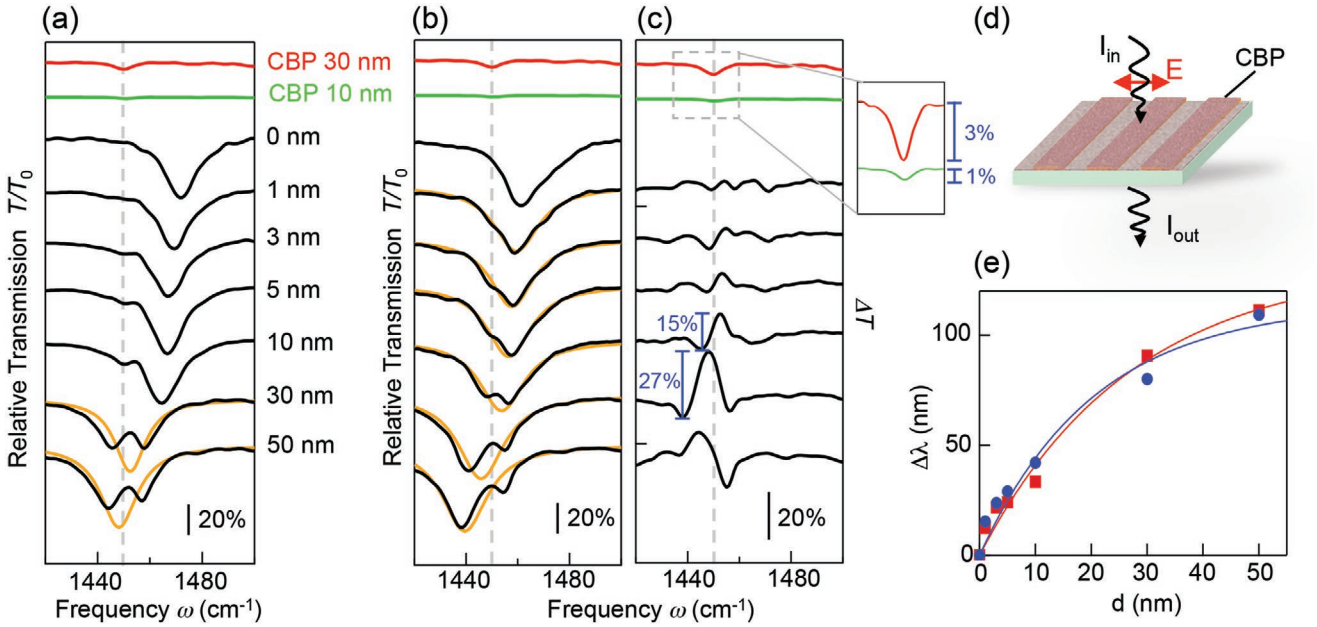

Figure 3. a) Transmission spectra of a set of h-BN* ribbon array ($D = 400$ nm, average width $w = 230$ nm) covered by CBP layers of various thicknesses (black curves). Red and green curves show spectra of 30 and 10 nm-thick CBP layers on a bare CaF_2 substrate. The grey dashed line marks the spectral position of the C—H vibration. The orange curves show spectra of the bare HPhP resonators, reconstructed via a coupled oscillators model fit. b) Same as panel (a), but for ribbon arrays with average width $w = 270$ nm. c) Spectral signature of the CBP layers on h-BN* arrays, obtained from panel (b). d) Sketch of the transmission spectroscopy experiment. e) Spectral shift $\Delta\lambda$ of the bare HPhP resonance as a function of the CBP layer thickness, d, for the set of arrays with $w = 230$ nm (red squares), and $w = 270$ nm. Fits of Equation (1) to data are plotted as continuous lines.

To quantify the enhancement of the CBP spectral signature, we plot $\Delta T = \frac{T}{T_0} - \frac{T_{\mathrm{HPhP}}}{T_0}$ for the various CBP layer thicknesses (Figure 3c) and compare the vibrational signature (indicated by blue bars) with the absorption dip for layers on the bare CaF_2 substrate. For the 10 nm-thick bare CBP layer, the vibrational signature amounts to around 1% of the transmission (see green spectrum). This signature increases to 15% when the 10 nm thick layer is placed on top of the ribbons. Analogously, the spectral signature of the 30 nm thick CBP layer (see red spectrum) increases from 3% to 27%. We note that the enhancement of the SEIRA signal of about one order of magnitude is comparable to that observed for CBP molecules on gold antennas.[33] On the other hand, the relative dip splitting is much stronger for the CBP molecules on the h-BN* antennas, which in the future should be taken into account for a more elaborated determination of the SEIRA signal enhancement factor.

To explore the potential of HPhP resonators for RI sensing, we analyze the spectral shift of the HPhP resonance, $\Delta\lambda$, as a function of the CBP layer thickness d. We perform this analysis in wavelength units for better comparison with literature results. Figure 3e (red squares and blue dots) shows $\Delta\lambda$ obtained from the spectra of the two h-BN* ribbon arrays with 230 and 270 nm ribbon width, respectively (Figure 3a,b). Although the spectral shift is clearly visible for even a 1 nm-thin CBP layer, a quantitative evaluation of the spectral shift requires some considerations. The conventional figure of merit (FOM) for RI sensing is defined as $\mathrm{FOM}_{\mathrm{bulk}} = \partial\lambda / \partial \mathrm{n}$, describing the shift of the resonance wavelength of a plasmonic mode when the refractive index n of the surrounding material is varied. However, it has been recently argued that this quantity does not represent the most significant FOM to evaluate the performance of RI sensors when nanometric-thin analyte layers are probed,[34,35] as the dielectric environment of the sensor is changed only in its close proximity. In this case, it is more appropriate to evaluate the surface sensitivity, which depends on the specific electric field distribution above the sensor surface and its decay length. In recent experiments using plasmonic nanostructures,[34,35] it has been proposed to quantify the plasmonic spectral shift $\Delta\lambda$ as a function of the thickness t of the analyte according to:

$$\Delta\lambda = m\,\Delta n\left(1 - e^{-\frac{2t}{l_{\mathrm{d}}}}\right) \tag{1}$$

where Δn is the variation of the refractive index due to the analyte and l_{d} the electric field decay length in a simplified scenario with a 1D field distribution along the vertical axis. In a more realistic scenario, the field distribution is highly inhomogeneous in 3D space and l_{d} corresponds to an effective decay length. The parameter m corresponds to the bulk FOM for the case $t \gg l_{\mathrm{d}}$. Within this framework, the so-called second-order surface sensitivity can be calculated as the second order derivative of the spectral shift $\Delta\lambda$,

$$\frac{\partial^2 \Delta\lambda}{\partial n\,\partial t} = \frac{2m}{l_{\mathrm{d}}}\,e^{-\frac{2t}{l_{\mathrm{d}}}} \tag{2}$$

The prefactor of this expression, $\frac{2m}{l_{\mathrm{d}}}$, which corresponds to the sensitivity for analyte thicknesses approaching zero, can be used to compare the performance of different thin layer RI sensors.[34,35,36] We thus fit Equation (1) to the $\Delta\lambda$ values plotted in Figure 3e, setting $\Delta n = 0.67$ according to the CBP non-dispersive dielectric background $\varepsilon_\infty = 2.8$.[15,32] The parameters extracted from the fits (solid lines in Figure 3e) are $m = 198$ nm/RIU and $l_{\mathrm{d}} = 54$ nm for the 230 nm wide h-BN* ribbons, and $m = 171$ nm/RIU and $l_{\mathrm{d}} = 41$ nm for the 270 nm wide h-BN* ribbons. We subsequently obtain $\frac{2m}{l_{\mathrm{d}}} = 7.3$ RIU^{-1} and $\frac{2m}{l_{\mathrm{d}}} = 8.3$ RIU^{-1}, respectively. These values are higher or similar to the ones reported for diffractively coupled plasmonic crystals in the visible range,[34,36] which makes h-BN* ribbon arrays promising candidates for mid-IR refractive index sensing.

5. Vibrational Strong Coupling with h-BN* Phonon-Polariton Resonators

In our recent work,[15] the coupling between CBP molecular vibrations and HPhPs in ribbons made of naturally abundant h-BN nearly reached the strong coupling regime, in which the original states mix, forming two new hybridized polaritonic states. The higher Q factors obtained with h-BN* nanoresonators could be decisive for fully reaching vibrational strong coupling. We thus repeated the experiment with a set of h-BN* ribbon arrays. We evaporated 30 nm of CBP on top of the arrays and measured IR transmission spectra (**Figure 4**a). All spectra show a double-dip structure, exhibiting an anti-crossing behavior when approaching the CBP vibrational mode at 1450 cm^{-1}. To verify strong coupling, the mere observation of anti-crossing in transmission spectra is not sufficient, as it does not necessarily imply a hybridization of the interacting modes. For a proper evaluation of the coupling regime, it is necessary to retrieve the coupling strength between the two modes, g, and compare it with the damping. To that end, we fitted to each spectrum the coupled harmonic oscillator model described above.

Fitting the spectrum of each ribbon array, we determined the coupling strength g, the bare HPhP eigenfrequency ω_{HPhP} and the damping parameter γ_{HPhP}. Note that the bare molecular vibrational eigenfrequency ω_{CBP} and the damping parameter γ_{CBP} were fixed according to the CBP dielectric function (see Sections S5 and S6 of Supporting Information). These parameters can be used to calculate the eigenfrequencies of hybrid states of the coupled system,[37] $\omega_\pm$, which are plotted in Figure 4b as a function of ω_{HPhP} (blue symbols, see Section S5, Supporting Information for details). The anti-crossing of the $\omega_\pm$ branches is a necessary condition for strong coupling and corresponds to the mathematical condition $C_1 \stackrel{\mathrm{def}}{=} \frac{|g|}{|\gamma_{\mathrm{HPhP}} - \gamma_{\mathrm{CBP}}|} > 0.25$.[38,39] Using the average values extracted from the fits ($g = 6.4$ cm^{-1}, $\gamma_{\mathrm{HPhP}} = 15.0$ cm^{-1}, $\gamma_{\mathrm{CBP}} = 8.5$ cm^{-1}) we obtain $C_1 \cong 1.0$, indicating strong coupling. Even the stricter condition $C_2 \stackrel{\mathrm{def}}{=} |g| / |\gamma_{\mathrm{HPhP}} + \gamma_{\mathrm{CBP}}| > 0.25$[38] is fulfilled, as we find $C_2 \cong 0.27$. This second condition was not fulfilled in the case of naturally abundant h-BN, as reported by Autore et al.[15] An alternative condition to verify strong coupling, also found in literature,[38] is based

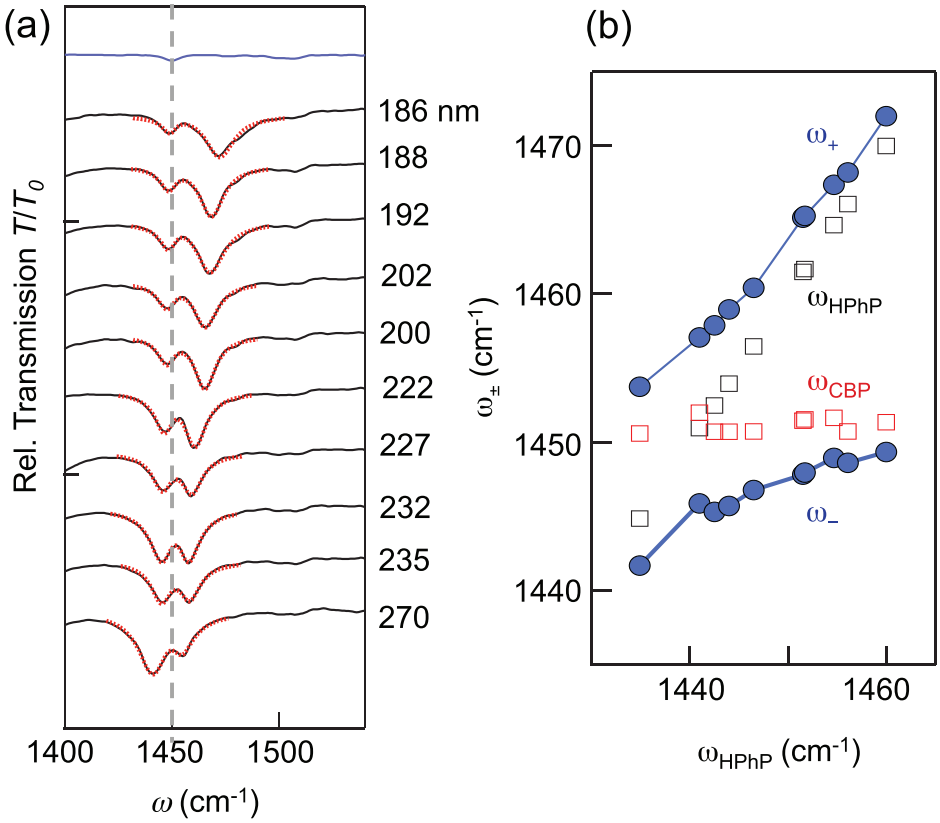

Figure 4. a) Relative transmission spectra of 32 nm-thick h-BN* ribbon arrays covered by a 30 nm thick CBP layer (black curves). The ribbon width in nm is indicated on the right side. Red curves show fits obtained with the coupled harmonic oscillator model. Blue curve represents the spectrum of a 30 nm thick CBP layer on a bare CaF_2 substrate. b) Eigenfrequencies $\omega_\pm$(blue dots), obtained from the fits shown in panel (a). The red and black open squares show the bare CBP vibration frequency, ω_{CBP}, and the bare HPhP resonance frequency, ω_{HPhP}, respectively, obtained from the fits shown in panel (a).

on verifying that the normal mode splitting at zero detuning is larger than the losses of the system, and can be expressed as $\omega_+ - \omega_- > \frac{\gamma_{HPhP}}{2} + \frac{\gamma_{CBP}}{2}$. This condition is fulfilled in our experiment, in which we obtain 12.6 cm^{-1} > 11.5 cm^{-1}. We corroborate our findings with electromagnetic simulations of the absorption of the CBP molecules on the h-BN* ribbons (see Section S6, Supporting Information), in which we observe a splitting of the absorption peak, which is a clear signature of strong coupling.[40]

6. Conclusion

In summary, we studied the fundamental infrared response of phonon-polaritonic nanoribbon arrays made of monoisotopic ^{10}B h-BN, as well as their potential for infrared sensing and strong coupling applications. Compared to ribbon arrays made of naturally abundant h-BN (fabricated within the same process), the monoisotopic h-BN ribbons exhibit phonon-polariton resonances of higher Q factors, promising superior performance in applications that require narrow-band resonances. Further, for higher-order modes in 90 nm thick resonators we found Q factors of up to 310. We also studied the performance of monoisotopic h-BN nanoribbons for simultaneous SEIRA spectroscopy and refractive index sensing. To that end, we deposited CBP layers of varying thickness onto the ribbons and analyzed the transmission spectra. We found that the CBP vibrational signature can be enhanced by about a factor of 10 compared to the vibrational signature of a CBP layer of comparable thickness. Regarding the refractive index sensing capabilities, we evaluated the surface sensitivity, which is the most relevant quantity to be considered when dealing with thin films of an analyte. The surface sensitivity of the h-BN ribbons was better or comparable to the ones reported for diffractively-coupled plasmonic crystals in the visible range.[34,36] The combined SEIRA and refractive index sensing capabilities demonstrate the promising potential of monoisotopic h-BN nanostructures to become a novel mid-infrared sensing platform, which could be improved by optimizing the resonator geometry or by enhancing the excitation efficiency of HPhP modes, for example, by combining them with metallic gratings or Salisbury screens.[41,42] Finally, the improved Q factor of monoisotopic h-BN resonators enabled strong coupling between the CBP molecular vibrations and the HPhP resonators, which was only achieved at its onset with naturally abundant h-BN nanoribbons.[15] In the future, one may exploit strong coupling between molecular vibrations and phononic resonators for the nanoscale modification of the chemical landscape[43,44,45] and the speed of chemical reactions,[46] opening new opportunities in the field of nanoscale selective catalysis and quantum optical chemistry.[47]

7. Experimental Section

Monoisotopic h-BN Crystal Growth Method: The ^{10}B enriched h-BN crystals were grown from metal flux method. A Ni-Cr-^{10}B powder mixture at respective 48 and 4 wt% was first loaded into an alumina crucible and placed in a single-zone furnace. The furnace was evacuated and then filled with N_2 and H_2 gases to a constant pressure of 850 Torr. During the reaction process, the N_2 and H_2 gases continuously flowed through the system at rates of 125 and 5 sccm, respectively. All the nitrogen in the hBN crystal originated from the flowing N_2 gas. H_2 gas was used to minimize oxygen and carbon impurities in the hBN crystal. After a dwell time of 24 h at 1550 °C, the hBN crystals were precipitated on the metal surface by cooling at a rate of 0.5 °C h^{-1} to 1525 °C, and then the system was quickly quenched to room temperature.

Fabrication of h-BN Ribbon Arrays: Large and homogeneous h-BN flakes were exfoliated and deposited on a CaF_2 substrate. h-BN nanoribbon arrays of different widths were fabricated from the h-BN flakes by high-resolution electron beam lithography using poly(methyl methacrylate)as a positive resist and subsequent chemical dry etching (see Ref. [15] for more details on the fabrication process).

Thermal Evaporation of CBP: 4,4′-bis(N-carbazolyl)-1,1′-biphenyl[48] with sublimed quality (99.9%) (Sigma Aldrich) was thermally evaporated in an ultra-high vacuum evaporator chamber (base pressure < 10^{-9} mbar), at a rate of 0.1 nm s^{-1} using a Knudsen cell.

Fourier Transform Infrared (FTIR) Micro-Spectroscopy Measurements: FTIR transmission measurements were performed using a Bruker Hyperion 2000 infrared microscope coupled to a Vertex 70 FTIR spectrometer (Bruker Optics GmbH, Germany). The radiation from a thermal source (Globar) was linearly polarized via a wire grid polarizer. The normal-incidence transmission spectra of the bare and molecule-coated h-BN arrays were recorded with a spectral resolution of 2 cm^{-1}. All measurements were taken at room temperature and ambient pressure, in an N_2-purged box.

Fitting Procedures for Uncoupled and Coupled HPhP Resonances: We fitted a Lorentzian line shape to each spectrum in Figure 1a,b to determine the resonance frequency ω_{HPhP} and the FWHM γ_{HPhP}. We used the formula:

$$\frac{T}{T_0} = 1 - \gamma_0 - \frac{A}{(\omega - \omega_{HPhP})^2 + \left(\frac{\gamma_{HPhP}}{2}\right)^2} \tag{3}$$

where γ_0 and A are further fitting parameters.

In order to fit the spectra of the coupled HPhP-CBP vibration, we used the model described in detail in our previous work.[15] The complete sets of parameters obtained by fitting are reported in the Supporting Information.

Electromagnetic Simulations: The spectral response of h-BN* nanostructures was studied via full-wave numerical simulations using the finite-elements method in frequency domain (COMSOL). The CaF_2 substrate was described by a constant ε_{CaF2} = 1.882, while the h-BN* dielectric permittivity was modeled according to $\varepsilon_a^{h\text{-}BN} = \varepsilon_{a,\infty}\left(1 + \frac{(\omega_a^{LO})^2 - (\omega_a^{TO})^2}{(\omega_a^{TO})^2 - \omega^2 - i\omega\gamma_a}\right)$, where $a = \parallel, \perp$ indicates the component parallel or perpendicular to the anisotropy axis. Simulations were run using the following parameters: $\varepsilon_{\parallel,\infty} = 2.8$, $\omega_\parallel^{TO} = 785$ cm^{-1}, $\omega_\parallel^{LO} = 845$ cm^{-1}, $\gamma_\parallel = 1$ cm^{-1}, $\varepsilon_{\perp,\infty} = 3.0$, $\omega_\perp^{TO} = 1395$ cm^{-1}, $\omega_\perp^{LO} = 1630$ cm^{-1}, and $\gamma_\perp = 2$ cm^{-1}.[17,20]

Supporting Information

Supporting Information is available from the Wiley Online Library or from the author.

Acknowledgements

The authors acknowledge funding from the Graphene Flagship (Core2 and Core3), the Spanish Ministry of Science and Innovation (projects MDM-2016-0618 of the Maria de Maeztu Units of Excellence Programme and national projects (RTI2018-094830-B-I00, RTI2018-094861-B-I00, and PID2019-107432GB-I00)), and the Basque Government (project GIU18/202, Ekartek project KK-2018/00001, IT1164-19, and PhD fellowships PRE_2018_2_0253 and PRE_2017_2_0052). The h-BN crystal growth was supported by the National Science Foundation, grant CMMI 1538127 and the II-VI Foundation.

Conflict of Interest

The authors declare no conflict of interest.

Keywords

boron nitride, phonon-polaritons, strong coupling, surface enhanced infrared absorption

Received: November 13, 2020
Revised: December 4, 2020
Published online: December 23, 2020

[1] M. L. Bongersma, P. G. Kik, *Surface Plasmon Nanophotonics*, Springer, New York **2010**.
[2] J. A. Schuller, E. S. Barnard, W. Cai, Y. C. Jun, J. S. White, M. L. Brongersma, *Nat. Mater.* **2010**, *9*, 193.
[3] A. I. Kuznetsov, A. E. Miroshnichenko, M. L. Brongersma, Y. S. Kivshar, B. Luk'yanchuk, *Science* **2016**, *354*, aag2472.
[4] F. J. G. de Abajo, *Science* **2013**, *339*, 917.
[5] J. D. Caldwell, L. Lindsay, V. Giannini, I. Vurgaftman, T. L. Reinecke, S. A. Maier, O. J. Glembocki, *Nanophotonics* **2015**, *4*, 44.
[6] R. Hillenbrand, T. Taubner, F. Keilmann, *Nature* **2002**, *418*, 159.
[7] J. D. Caldwell, O. J. Glembocki, Y. Francescato, N. Sharac, V. Giannini, F. J. Bezares, J. P. Long, J. C. Owrutsky, I. Vurgaftman, J. G. Tischler, V. D. Wheeler, N. D. Bassim, L. M. Shirey, R. Kasica, S. A. Maier, *Nano Lett.* **2013**, *13*, 3690.
[8] P. N. Li, X. S. Yang, T. W. W. Maß, J. Hanss, M. Lewin, A.-K. U. Michel, M. Wuttig, T. Taubner, *Nat. Mater.* **2016**, *15*, 870.
[9] N. C. Passler, C. R. Gubbin, T. G. Folland, I. Razdolski, D. S. Katzer, D. F. Storm, M. Wolf, S. De Liberato, J. D. Caldwell, A. Paarmann, *Nano Lett.* **2018**, *18*, 4285.
[10] R. Esteban, J. Aizpurua, G. W. Bryant, *New J. Phys.* **2014**, *16*, 013052.
[11] J. D. Caldwell, K. Novoselov, *Nat. Mater.* **2015**, *14*, 364.
[12] S. Dai, Z. Fei, Q. Ma, A. S. Rodin, M. Wagner, A. S. McLeod, M. K. Liu, W. Gannett, W. Regan, K. Watanabe, T. Taniguchi, M. Thiemens, G. Dominguez, A. H. Castro Neto, A. Zettl, F. Keilmann, P. Jarillo-Herrero, M. M. Fogler, D. N. Basov, *Science* **2014**, *343*, 1125.
[13] E. Yoxall, M. Schnell, A. Y. Nikitin, O. Txoperena, A. Woessner, M. B. Lundeberg, F. Casanova, L. E. Hueso, F. H. L. Koppens, R. Hillenbrand, *Nat. Photonics* **2015**, *9*, 674.
[14] J. D. Caldwell, A. Kretinin, Y. G. Chen, V. Giannini, M. M. Fogler, Y. Francescato, C. T. Ellis, J. G. Tischler, C. R. Woods, A. J. Giles, M. Hong, K. Watanabe, T. Taniguchi, S. A. Maier, K. S. Novoselov, *Nat. Commun.* **2014**, *5*, 5221.
[15] M. Autore, P. Li, I. Dolado, F. J. Alfaro-Mozaz, R. Esteban, A. Atxabal, F. Casanova, L. E. Hueso, P. Alonso-Gonzalez, J. Aizpurua, A. Y. Nikitin, S. Velez, R. Hillenbrand, *Light: Sci. Appl.* **2018**, *7*, 17172.

[16] I. Dolado, F. J. Alfaro-Mozaz, P. Li, E. Nikulina, A. Bylinkin, S. Liu, J. H. Edgar, F. Casanova, L. E. Hueso, P. Alonso-González, S. Vélez, A. Y. Nikitin, R. Hillenbrand, *Adv. Mater.* **2020**, *32*, 1906530.
[17] F. J. Alfaro-Mozaz, P. Alonso-González, S. Vélez, I. Dolado, M. Autore, S. Mastel, F. Casanova, L. E. Hueso, P. Li, A. Y. Nikitin, R. Hillenbrand, *Nat. Commun.* **2017**, *8*, 15624.
[18] P. Li, I. Dolado, F. J. Alfaro-Mozaz, F. Casanova, L. E. Hueso, S. Liu, J. H. Edgar, A. Y. Nikitin, S. Vélez, R. Hillenbrand, *Science* **2018**, *359*, 892.
[19] F. Neubrech, C. Huck, K. Weber, A. Pucci, H. Giessen, *Chem. Rev.* **2017**, *117*, 5110.
[20] F. Neubrech, A. Pucci, T. W. Cornelius, S. Karim, A. García-Etxarri, J. Aizpurua, *Phys. Rev. Lett.* **2008**, *101*, 157403.
[21] A. J. Giles, S. Dai, I. Vurgaftman, T. Hoffman, S. Liu, L. Lindsay, C. T. Ellis, N. Assefa, I. Chatzakis, T. L. Reinecke, J. G. Tischler, M. M. Fogler, J. H. Edgar, D. N. Basov, J. D. Caldwell, *Nat. Mater.* **2018**, *17*, 134.
[22] S. Liu, R. He, L. Xue, J. Li, B. Liu, J. H. Edgar, *Chem. Mater.* **2018**, *30*, 6222.
[23] A. J. Giles, S. Dai, O. J. Glembocki, A. V. Kretinin, Z. Sun, C. T. Ellis, J. G. Tischler, T. Taniguchi, K. Watanabe, M. M. Fogler, K. S. Novoselov, D. N. Basov, J. D. Caldwell, *Nano Lett.* **2016**, *16*, 3858.
[24] L. V. Brown, M. Davanco, Z. Sun, A. Kretinin, Y. Chen, J. R. Matson, I. Vurgaftman, N. Sharac, A. J. Giles, M. M. Fogler, T. Taniguchi, K. Watanabe, K. S. Novoselov, S. A. Maier, A. Centrone, J. D. Caldwell, *Nano Lett.* **2018**, *18*, 1628.
[25] A. Ambrosio, M. Tamagnone, K. Chaudhary, L. A. Jauregui, P. Kim, W. L. Wilson, F. Capasso, *Light: Sci. Appl.* **2018**, *7*, 27.
[26] R. Berte, C. R. Gubbin, V. D. Wheeler, A. J. Giles, V. Giannini, S. A. Maier, S. De Liberato, J. D. Caldwell, *ACS Photonics* **2018**, *5*, 2807.
[27] I. M. Pryce, Y. A. Kelaita, K. Aydin, H. A. Atwater, *ACS Nano* **2011**, *5*, 8167.
[28] B. Vasić, G. Isić, R. Gajić, *J. Appl. Phys.* **2013**, *113*, 013110.
[29] F. B. Barho, F. Gonzalez-Posada, M. J. Milla-Rodrigo, M. Bomers, L. Cerutti, T. Taliercio, *Opt. Express* **2016**, *24*, 16175.
[30] X. Chen, C. Wang, Y. Yao, C. Wang, *ACS Nano* **2017**, *11*, 8034.
[31] Z. Li, Y. Zhu, Y. Hao, M. Gao, M. Lu, A. Stein, A.-H. A. Park, J. C. Hone, Q. Lin, N. Yu, *ACS Photonics* **2019**, *6*, 501.
[32] A. Delga, J. Feist, J. Bravo-Abad, F. J. Garcia-Vidal, *Phys. Rev. Lett.* **2014**, *112*, 253601.
[33] J. Vogt, C. Huck, F. Neubrech, A. Toma, D. Gerbert, A. Pucci, *Phys. Chem. Chem. Phys.* **2015**, *17*, 21169.
[34] J. Li, J. Ye, C. Chen, L. Hermans, N. Verellen, J. Ryken, H. Jans, W. Van Roy, V. V. Moshchalkov, L. Lagae, P. Van Dorpe, *Adv. Opt. Mater.* **2015**, *3*, 176.
[35] T. Wenger, G. Viola, J. Kinaret, M. Fogelström, P. Tassin, *2D Mater.* **2017**, *4*, 025103.
[36] J. Li, J. Ye, C. Chen, Y. Li, N. Verellen, V. V. Moshchalkov, L. Lagae, P. Van Dorpe, *ACS Photonics* **2015**, *2*, 425.
[37] K. Hennessy, A. Badolato, M. Winger, D. Gerace, M. Atatüre, S. Gulde, S. Fält, E. L. Hu, A. Imamoglu, *Nature* **2007**, *445*, 896.
[38] P. Törmä, W. L. Barnes, *Rep. Prog. Phys.* **2015**, *78*, 013901.
[39] D. Melnikau, R. Esteban, D. Savateeva, A. Sánchez-Iglesias, M. Grzelczak, M. K. Schmidt, L. M. Liz-Marzán, J. Aizpurua, Y. P. Rakovich, *J. Phys. Chem. Lett.* **2016**, *7*, 354.
[40] T. J. Antosiewicz, S. P. Apell, T. Shegai, *ACS Photonics* **2014**, *1*, 454.
[41] S. Kim, M. S. Jang, V. W. Brar, K. W. Mauser, L. Kim, H. A. Atwater, *Nanoletters* **2018**, *18*, 971.
[42] I. H. Lee, D. Yoo, P. Avouris, T. Low, S. H. Oh, *Nat. Nanotechnol.* **2019**, *14*, 313.
[43] S. R. Casey, J. R. Sparks, *J. Phys. Chem. C* **2016**, *120*, 28138.
[44] A. Shalabney, J. George, H. Hiura, J. A. Hutchison, C. Genet, P. Hellwig, T. W. Ebbesen, *Angew. Chem., Int. Ed.* **2015**, *54*, 7971.
[45] A. Thomas, L. Lethuillier-Karl, K. Nagarajan, R. M. A. Vergauwe, J. George, T. Chervy, A. Shalabney, E. Devaux, C. Genet, J. Moran, T. W. Ebbesen, *Science* **2019**, *363*, 615.
[46] A. Thomas, J. George, A. Shalabney, M. Dryzhakov, S. J. Varma, J. Moran, T. Chervy, X. Zhong, E. Devaux, C. Genet, J. A. Hutchinson, T. W. Ebbesen, *Angew. Chem.* **2016**, *128*, 11634.
[47] B. S. Simpkins, K. P. Fears, W. J. Dressick, B. T. Spann, A. D. Dunkelberger, J. C. Owrutsky, *ACS Photonics* **2015**, *2*, 1460.
[48] T. Glaser, S. Beck, B. Lunkenheimer, D. Donhauser, A. Köhn, M. Kröger, A. Pucci, *Org. Electron.* **2013**, *14*, 575.